


Cite this: *J. Mater. Chem. A*, 2023, 11, 16321

# Flexible covalent organic framework membranes with linear aliphatic amines for enhanced organic solvent nanofiltration†

Biswajit Mishra and Bijay P. Tripathi \*

Covalent organic framework (COF) based membranes hold great promise for organic solvent nanofiltration (OSN) due to their unique molecular arrangement, well-defined porous network, and broader solvent tolerance. However, scaling up their fabrication on porous supports without compromising these properties presents many challenges. In this study, COF membranes are fabricated on a porous support using liquid–liquid interfacial polymerization. The pore size and chemistry of the COF membranes are rationally modified by covalently bridging different aliphatic diamines with varying amine groups. The growth process of the COFs nanofilm is thoroughly studied using morphology and chemical structures analysis, which confirms  $\beta$ -ketoenamine bond formation between both monomers. Next, the COFs film is transferred to a porous support and thoroughly investigated before its application in OSN. The fabricated COF membranes display superior solvent permeance and precise molecular separation compared to conventional nanofiltration membranes. They also demonstrate substantial fouling resistance in both static and dynamic conditions. Furthermore, the COF membranes show good operational stability when subjected to continuous solvent permeation for 24 h without any surface defects or disruption in permeation activity. These results demonstrate the potential for synthesizing linear aliphatic diamine-based COFs and their membranes *via* facile liquid–liquid interfacial polymerization for various membrane filtration applications.

Received 5th May 2023  
Accepted 11th July 2023

DOI: 10.1039/d3ta02683c

[rsc.li/materials-a](https://rsc.li/materials-a)

## 1. Introduction

Approximately 15% of the world's energy consumption is devoted to separation processes in various industrial sectors.<sup>1–3</sup> These processes often use thermal techniques such as distillation, evaporation, and adsorption, which require significant amounts of energy.<sup>4,5</sup> However, membrane technology is known for its low energy consumption, efficient separation, small carbon footprint, and environmental friendliness, making it popular in industries such as chemicals, drugs, and medicine.<sup>6–8</sup> Membrane based nanofiltration (NF) is an emerging technology for high-throughput charge and size based molecular separations.<sup>9,10</sup> Although NF membranes can effectively separate solutes with a molecular weight of 200–2000 Da, their applications are limited to aqueous environments.<sup>11,12</sup> In contrast, organic solvent nanofiltration (OSN) is a newer technology that can effectively separate solutes from various solvent systems, making it an attractive option for chemical industries due to its lower energy consumption.<sup>13,14</sup>

However, developing materials for OSN membranes with chemical resistance under a wide range of organic solvents, long-term filtration performance, and operation stability remains a challenge. To address this challenge, OSN membranes must meet requirements such as being stable under a wide range of solvents (polar and nonpolar), having a small pore diameter (typically below 2 nm) with uniform pore size distribution, easy fabrication and scale-up, and a thinner selective layer thickness.<sup>14,15</sup> Current polymeric NF membranes have limited chemical resistance and non-uniform pore size distribution, while ceramic membranes are too expensive.<sup>16,17</sup> Moreover, the permeability and selectivity of these membranes are limited due to their non-uniform, broader pore-size distribution.<sup>18,19</sup> Therefore, there is a need for advancements in the design and fabrication of OSN membranes with enhanced chemical resistance, better permeability-selectivity, uniform pore size distribution, and cost-effectiveness.

Covalent organic frameworks (COFs) are a rapidly growing class of crystalline porous materials constructed through reticular chemistry, where organic building blocks are connected by strong covalent bonds in a periodic manner.<sup>20–22</sup> These materials, which are synthesized using lightweight elements such as C, N, O, and B, can be classified as one-, two-, or three-dimensional based on their design.<sup>23</sup> Due to their ordered aperture sizes, high surface area, layered channels, and

Functional Materials & Membranes Laboratory, Department of Materials Science and Engineering, Indian Institute of Technology Delhi, Hauz Khas, New Delhi 110016, India. E-mail: [bpatripathi@mse.iitd.ac.in](mailto:bpatripathi@mse.iitd.ac.in); [drbptripathi@gmail.com](mailto:drbptripathi@gmail.com)

† Electronic supplementary information (ESI) available. See DOI: <https://doi.org/10.1039/d3ta02683c>

structural diversity, COFs have found applications in gas separation and storage, catalysis, electrochromic devices, adsorption, and metal-ion batteries.<sup>24–27</sup> Their higher crystallinity and molecular architecture make them stable under a wide range of solvents, acids, and bases, making them an attractive material for developing high-performance OSN membranes.<sup>3,28–30</sup> Unlike graphene and other polymeric membranes, COFs have inherent permanent porosity without any post-treatment, which makes them suitable for controlling pore size by selecting appropriate building blocks.<sup>17,31–33</sup>

Traditionally, COFs are synthesized using solvothermal and microwave methods that produce bulk powders, which limit their application in membrane technology. Although these powders have good crystallinity and a uniform porous structure, it is challenging to transform them into stable films with controlled pore size and distribution. COF membranes prepared by conventional methods, such as vacuum filtration, result in random stacking and uneven pore-size size distribution, which hinders their application in NF. Various fabricating strategies, such as solvent-assisted exfoliation, vapor-assisted conversion, layer-by-layer stacking, and *in situ* growth on a porous substrate, have been developed to prepare COF membranes, but scaling up and achieving defect-free membranes remains challenging.<sup>34</sup> So far, only a few techniques have been developed to prepare large-area flexible COF films suitable for OSN applications.

Interfacial polymerization (IP) is gaining tremendous attention for its simplicity and large-scale applicability in fabricating self-standing COF membranes.<sup>4,35</sup> During this process, the polymerization occurs at liquid–air or liquid–liquid interfaces. The selective layer of COF-based NF membranes is formed by IP, which is later transferred to a porous membrane support. In a typical imine-based IP process, amine monomers in an aqueous solution diffuse into an organic solvent phase at the interface, where they react with aryl aldehydes to form a continuous film. However, COF membranes require more precautions during the IP process than conventional polyamide membranes due to their regular molecular architecture and a higher degree of crystallinity. One disadvantage of the IP process is that a longer polymerization time is needed to achieve better crystallinity of the COF membrane, often resulting in a thicker COF layer. Membranes with thin selective layers are highly desirable for OSN to gain better control over permeability and selectivity. Recent studies have shown that by choosing an appropriate catalyst, such as scandium triflate, the crystallinity of COFs can be achieved at a lower IP time without any additional steps.<sup>36</sup> Poor solubility of aromatic diamines in water is another issue that could limit the membrane forming process. Chen and co-workers have overcome this issue by dissolving the two monomers in the same solvent instead of dissolving them in two separate solvents, resulting in the preparation of a continuous large area COF membrane.<sup>37</sup> COFs are traditionally synthesized by the coupling reaction between building blocks consisting of aromatic backbone. However, replacing the aromatic backbone with a non-aromatic one has not been explored much.<sup>38</sup> In this study, the aim is to construct COFs using aliphatic monomers as structurally flexible building

blocks, which can form disordered molecular islands and have the ability to produce continuous networks resulting from the reactions of aldehydes and aliphatic diamines. The use of aliphatic diamines could be a promising approach for preparing versatile COF membranes.

Herein, we have successfully fabricated COF membranes using liquid–liquid interfacial polymerization and different aliphatic amines. The effect of polymerization time on film thickness was studied, and the COF layer was shown to have good mechanical strength, crystallinity, flexibility, and high solvent tolerance. The fabricated COFs showed uniform pore size distribution with higher surface area, and the pore size increased with the length of the diamine chain. Subsequently, the developed COF membranes were utilized for OSN applications and exhibited exceptional performance in solvent permeance, solute rejection, and long-term operational stability. These findings suggest that COFs have vast design possibilities and could be promising candidates for various applications.

## 2. Results and discussion

### 2.1 Synthesis of aliphatic diamine based thin-film COF membranes

$\beta$ -Ketoenamine-based COF thin films were fabricated through a liquid–liquid IP strategy as shown in Fig. 1A. Highly stable and chemically robust COF thin films were produced at the interface by reacting aldehyde 2,4,6-triformylphloroglucinol and different chain length diamines (EDA, DETA, TETA) in the presence of scandium triflate. Scandium triflate was chosen as the catalyst due to its resistance to water and ability to accelerate imine formation only at the interface, even when both monomers are dissolved in the organic phase.<sup>36,39,40</sup> The detailed synthesis methodology is explained in the experimental section of the ESI (Section S1.2.2†). The COF layer thickness was controlled by varying the IP time. COFs were formed at the interface by the downward diffusion of TFG and diamines and their reaction in the presence of the catalyst (scandium triflate) in the aqueous phase. The film thickness control experiments were performed using TFG and EDA and replicated in all other cases.

The successful formation of the designed COF frameworks and the presence of  $\beta$ -ketoenamine linkage were confirmed by cross-polarization magic angle spinning (CP/MAS) <sup>13</sup>C solid-state NMR, as shown in Fig. S4(A–C) (ESI†). The absence of an aldehydic carbonyl carbon peak (which generally appears at ~193 ppm) and the appearance of a new resonance peak at ~183 ppm indicates the complete consumption of aldehydic precursor to form a stable keto product (>C=O) *via* tautomerization. In addition, all the COFs displayed sharp signals at ~105 ppm and ~155 ppm, indicating the presence of exocyclic (C=C) and iminic carbons, respectively.<sup>41</sup> The aliphatic carbons of the diamine linkers resonated at a lower signal around 40–50 ppm, confirming the successful formation of aliphatic diamine-linked COFs.

The thickness and surface texture of COF thin films were examined using FE-SEM, AFM, and ellipsometry techniques at various IP times. After a set period of IP, the films were

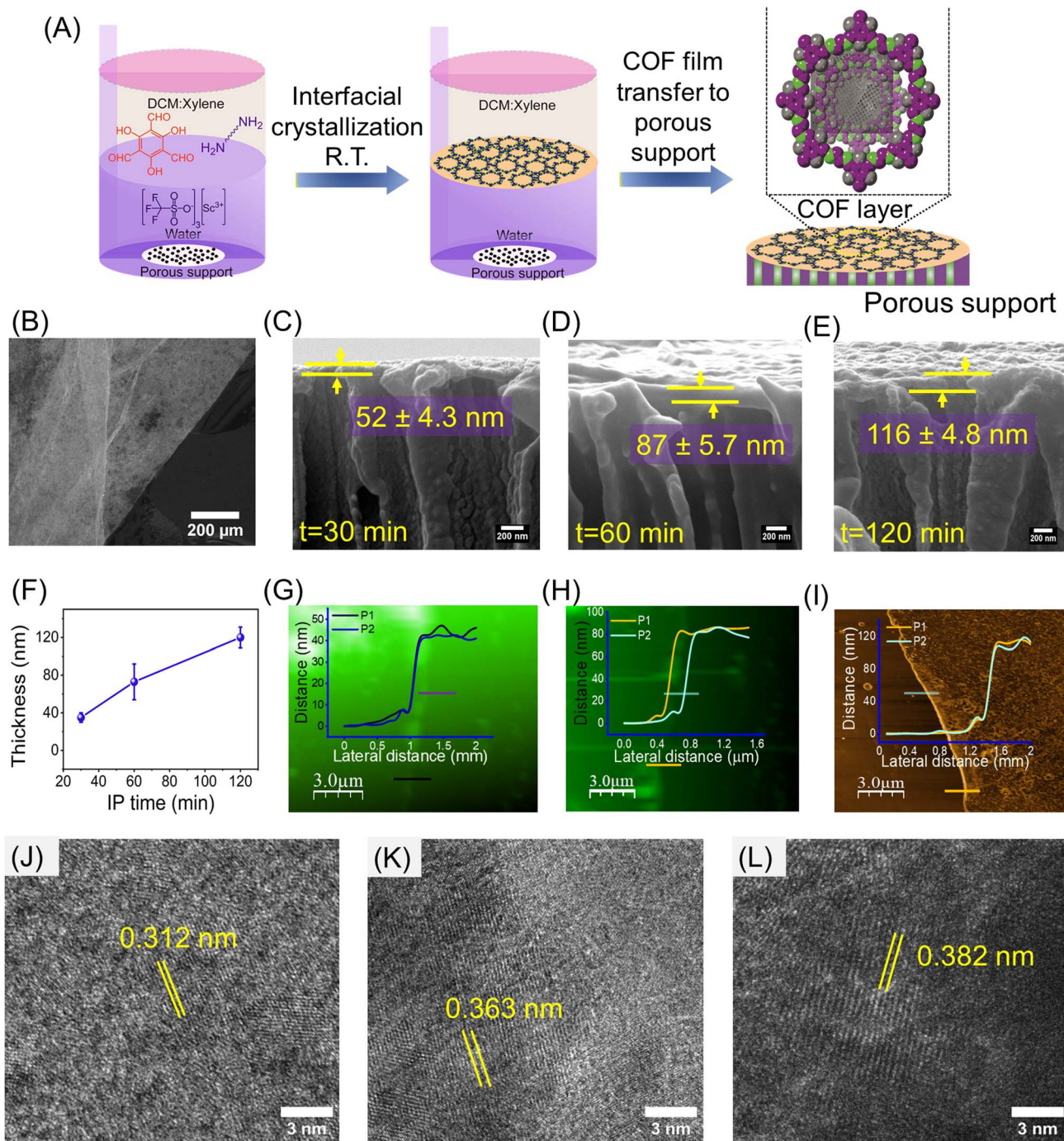


**Fig. 1** Synthesis procedure, growth mechanism, and morphology of COF films. (A) Schematic fabrication process for COF-based membranes and the thin film transfer process to a porous membrane support, (B) optical microscopy image of TFG-EDA on silicon wafer, (C–E) cross-sectional FE-SEM images demonstrating the thickness of TFG-EDA thin film at different interfacial polymerization times, (F) growth of film thickness with time measured using ellipsometry, and (G–I) AFM images showing the growth of film thickness at different polymerization times, (J–L) high-resolution TEM images of TFG-EDA, TFG-DETA, and TFG-TETA membranes (the interfacial films were removed, dispersed, and drop-cast on a TEM grid).

transferred to silicon wafers for AFM analysis, and the COF layer thickness on PET support was obtained using FESEM cross-sectional analysis. The optical image shows the formation of a continuous large area TFG-EDA thin film on a silicon wafer support (Fig. 1B). The thickness of the COF layer was observed

to increase from ~50 nm to ~116 nm as the IP time was increased from 30 min to 120 min due to the stacking of individual COF nanosheets (Fig. 1C–E). Ellipsometry analysis also supported this observation (Fig. 1F). The faster formation of the thin film on the support can be attributed to the presence of



both monomers in the same solvent phase, leading to an easier reaction. Surface FE-SEM analysis confirms the stacking of multiple COF layers over the membrane support, as evidenced by an initial wrinkle pattern that became denser with increasing interfacial time. Moreover, we did not observe any cracks or defects over a larger area (Fig. S5, ESI†). We performed similar IP experiments using DETA and TETA as diamines, with a fixed duration of 120 min. After 120 minutes of interfacial polymerization, the thickness of TFG-EDA, TFG-DETA, and TFG-TETA layer was measured to be  $116 \pm 4$  nm,  $120 \pm 5$  nm, and  $115 \pm 6$  nm, respectively (Fig. S3, ESI†). The FE-SEM, TEM, and AFM images of TFG-DETA and TFG-TETA membranes (Fig. S6, ESI†) reveal a continuous thin film without surface defects for all COFs. All COFs exhibited a wrinkled morphology, likely due to the slow evaporation of high boiling point xylene or the presence of an aliphatic diamine moiety enhancing molecular flexibility. After 72 h of IP, the film was removed, dispersed, and mounted on a TEM grid to visualize the morphology and crystallinity of COF membranes. As shown in Fig. 1J–L, high-resolution TEM images of COF thin films confirm the crystallinity of COF and the interplanar spacing was found to be 0.312, 0.363 and 0.382 nm for TFG-EDA, TFG-DETA, and TFG-TETA, respectively.

## 2.2 Characterization of COFs thin films

The formation of COFs based on  $\beta$ -Ketoenamine linkage was investigated using Fourier transform infrared (FT-IR) spectroscopy and XPS analysis. In the FTIR spectra, all the COF membranes exhibited prominent absorption bands at  $\sim 1620$   $\text{cm}^{-1}$  and  $\sim 1255$   $\text{cm}^{-1}$ , corresponding to the C=O and C–N linkages of  $\beta$ -ketoenamine, respectively.<sup>34,42,43</sup> Additionally,

the disappearance of amine (N–H, 3400–3200  $\text{cm}^{-1}$ ) and aldehydic carbonyl (C=O, 1651  $\text{cm}^{-1}$ ) peaks reveals the complete consumption of the starting precursors (Fig. S7(A–C), ESI†). The XPS survey spectra of all COFs confirmed the presence of C, N, and O, ensuring the absence of other impurities. As expected, an increase of N content from TFG-EDA to TFG-TETA was also observed (Fig. S8, ESI†). The high-resolution XPS spectra of individual elements were deconvoluted to confirm the possible chemical bonding in all the synthesized COFs. Specifically, the N 1s spectra shown in Fig. 2A–C exhibited a prominent peak at  $\sim 400.1$  eV, confirming the presence of an enamine nitrogen (C–NH) linkage.<sup>43</sup> The deconvoluted O 1s and C 1s spectra of all the COFs are shown in Fig. S8 (ESI†). In the O 1s spectra, the peaks at  $\sim 532.5$  and  $\sim 530.3$  eV were assigned to the C=O and C–OH linkage of  $\beta$ -ketoenamine-linked COFs. For the C 1s spectra, deconvolution analysis revealed five distinct peaks centered at  $\sim 283.5$ , 284.1, 284.8, 285.8 and 288.2 eV, corresponding to C=N,  $\text{sp}^2$  (C=C),  $\text{sp}^3$  (C–C), C–N and C–O linkages, respectively.<sup>44</sup>

The synthesized COFs' permanent and tunable porosity nature is essential for molecular separation applications. The porosity and texture properties were evaluated using  $\text{N}_2$  adsorption/desorption measurements at 77 K, as shown in Fig. 2D–F. All synthesized COFs exhibited a type 1 Brunauer–Emmett–Teller (BET) isotherm, with a rapid  $\text{N}_2$  adsorption feature observed at lower pressure ranges, indicating the microporous nature of all COFs. The surface areas of synthesized COFs were evaluated using the multi-point BET method (within the pressure range  $P/P_0$  of 0.04–0.25) and found to be 587, 697, and 591  $\text{m}^2 \text{g}^{-1}$ , respectively (Fig. S9, ESI†). The pore volume of TFG-EDA, TFG-DETA, and TFG-TETA was found to be

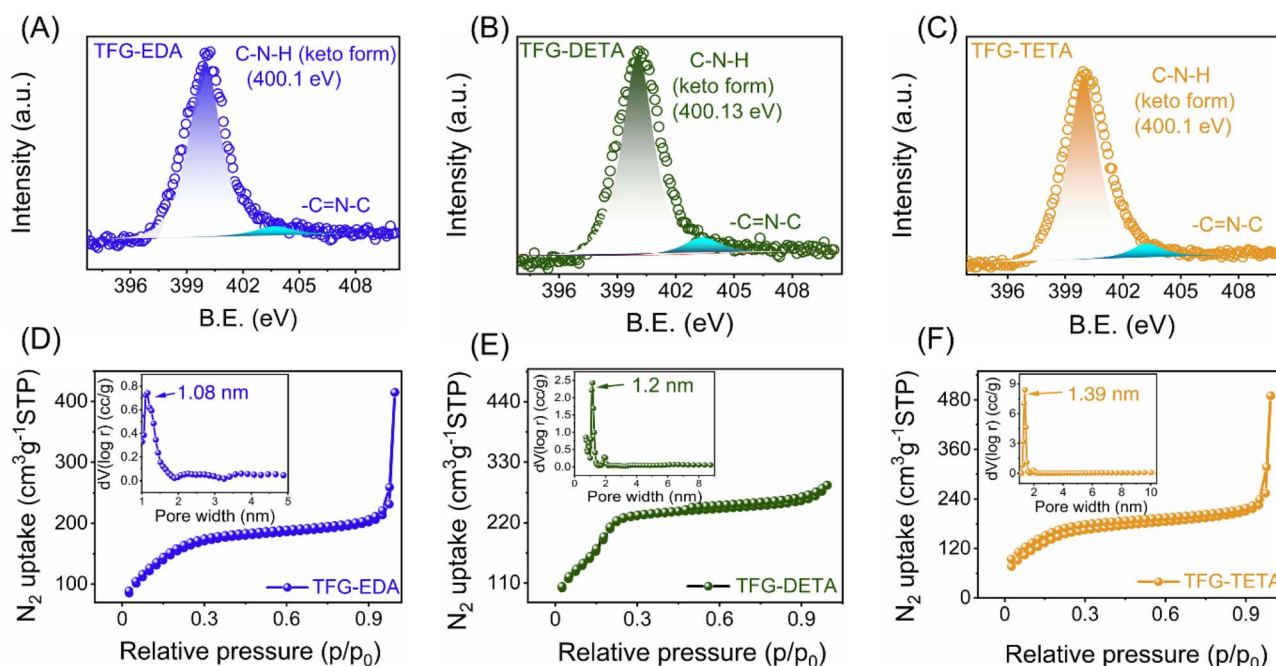


Fig. 2 XPS and BET characterization of TFG-EDA, TFG-DETA, and TFG-TETA thin films. (A–C) Show the deconvoluted N 1s spectra for TFG-EDA, TFG-DETA, and TFG-TETA. (D–F)  $\text{N}_2$  adsorption/desorption isotherm for TFG-EDA, TFG-DETA, and TFG-TETA, respectively.

0.341, 0.395, and  $0.39 \text{ cm}^3 \text{ g}^{-1}$ , respectively. Nonlocal density functional theory (NL-DFT) calculations were used to assess the pore-size distribution of COFs. The results indicated the presence of a narrow pore size distribution, with pore sizes of 1.08, 1.2, and 1.39 nm for TFG-EDA, TFG-DETA, and TFG-TETA thin films, respectively. The increasing pore-size trend correlates with an increase in the molecular diameter of diamine. Further, chemical, and thermal stability were necessary as it determines the robustness of COF thin films. The thermal stability of synthesized COFs was assessed using thermogravimetric analysis (TGA), and results are shown in Fig. S10 (ESI†). The TGA thermograms suggest that the COF frameworks exhibit thermal stability up to  $\sim 450 \text{ }^\circ\text{C}$ , comparable to previously reported aromatic COFs synthesized using a solvothermal approach.<sup>45,46</sup>

The crystal structures of TFG-EDA, TFG-DETA, and TFG-TETA were studied using the powder X-ray diffraction (PXRD) technique. Thinner COF layer membranes on PET support did not exhibit any crystalline pattern, likely due to their lower thickness, which was also reported in previous studies for interfacially crystallized thinner COF membranes.<sup>39,47</sup> A broad diffraction peak at  $22\text{--}29^\circ$  corresponding to the (001) plane of the COF layer was observed in the case of COF membranes obtained after 120 min of IP, resulting from the stacking of individual COFs on the support (Fig. S11, ESI†). To study the influence of interfacial polymerization time on the crystallization process COFs, XRD analysis was conducted at different time intervals, as shown in Fig. S12 (ESI†). Up to 120 minutes of interfacial polymerization, no significant peaks were observed in the XRD pattern. However, after 120 minutes of polymerization, two distinct diffraction peaks appeared at  $\sim 3.7^\circ$  and  $26^\circ$ , corresponding to (100) and (001) crystal planes, respectively, confirming the formation of crystalline framework structure in the COFs. These observations align with previous literature reports on COF synthesis and crystallization.<sup>48,49</sup> However, all synthesized free-standing COF films obtained after 72 h IP demonstrated a better crystalline pattern. PXRD patterns of TFG-EDA, TFG-DETA, and TFG-TETA showed two distinct diffraction peaks at  $\sim 3.7^\circ$  and  $25^\circ$  corresponding to the (100) and (001) planes, indicating lateral (in-plane) and vertical (stacked) growth of the COFs. Minor diffraction peaks at  $\sim 6.5^\circ$  and  $\sim 11.7^\circ$  were also observed, attributed to the (200) and (210) reflection planes, respectively. No other significant diffraction peaks were detected in the PXRD spectra, except for slight peak broadening at around  $25^\circ$ , which may be due to the inherent flexibility of aliphatic diamine-based COFs. These findings confirm the formation of well-defined crystalline covalent organic frameworks *via* interfacial polymerization, using scandium triflate as a catalyst. The diffraction patterns are consistent with previously reported COFs.<sup>50–54</sup> Further, structural simulation was performed using the materials studio to elucidate the crystalline structure of synthesized COF thin films. The structural models of the COFs were constructed using materials studio, and their geometries were optimized using the Forcite model with a universal force field. The experimental PXRD pattern and simulated profiles, along with the residual values for TFG-EDA, TFG-DETA, and TFG-TETA, are shown in Fig. 3A–C. The structural simulation study revealed that crystallized in

the P1 space group with two-dimensional eclipsed AA stacking (Fig. S13, ESI†). In addition, Pawley refinement elucidated an imperceptible difference between the experimental and simulated diffraction patterns. The unit cell parameters for TFG-EDA were calculated using Pawley refinement based on experimental data as  $a = 19.78 \text{ \AA}$ ,  $b = 30.54 \text{ \AA}$ ,  $c = 3.53 \text{ \AA}$ ,  $\alpha = 92.08^\circ$ ,  $\beta = 92.02^\circ$ , and  $\gamma = 121.59^\circ$ , with residual  $R_{\text{wp}} = 2.81\%$  and  $R_p = 1.86\%$ . For TFG-DETA, the parameters were  $a = 25.05 \text{ \AA}$ ,  $b = 28.24 \text{ \AA}$ ,  $c = 3.57 \text{ \AA}$ ,  $\alpha = 85.9^\circ$ ,  $\beta = 84.27^\circ$ , and  $\gamma = 110.7^\circ$  with residual  $R_p = 3.92\%$ ,  $R_{\text{wp}} = 5.88\%$ . For TFG-TETA, the parameters were  $a = 31.58 \text{ \AA}$ ,  $b = 33.61 \text{ \AA}$ ,  $c = 5.99 \text{ \AA}$ ,  $\alpha = 90.5^\circ$ ,  $\beta = 91.2^\circ$ , and  $\gamma = 109.8^\circ$  with residual  $R_p = 2.16\%$ ,  $R_{\text{wp}} = 2.62\%$ . The structural refinement data revealed that TFG-EDA, TFG-DETA, and TFG-TETA possess a well-defined crystallinity with an ordered hexagonal porous architecture (shown in Section S13, ESI†).<sup>29,55</sup> The experimental PXRD pattern shows good agreement with the simulated pattern, as indicated by low residual values and negligible profile differences. The distance between two adjacent COF layers was calculated from the transverse direction and found to be 0.316, 0.32, and 0.323 nm for TFG-EDA, TFG-DETA, and TFG-TETA, respectively.

To support the PXRD data, small angle X-ray scattering was performed on the synthesized COFs to obtain information on the crystallinity and porous nature of the thin films. As shown in Fig. 3D–F, the wider and clear scattering patterns with rings for all synthesized COFs indicate the crystallinity nature, which correlates with the PXRD data.<sup>55</sup> The corresponding scattering spectra displayed by COFs around  $\sim 0.02 \text{ nm}^{-1}$  matched well with the 100 facets of the crystal.<sup>56</sup> The higher scattering intensities for all synthesized COFs describe their higher porosity nature. The scattering intensity is proportional to a negative power of  $Q$  and can be used to model the scattering curves ( $I(q) = Aq^{-\alpha} + B$ ), where  $A$  is the constant and  $\alpha$  is the power exponent. The obtained power law exponent ( $\alpha < 3$ ) for all COFs indicates the lamellar morphology of COFs originating from the stacking of individual COF nanosheets.<sup>57,58</sup> Similar sheet-like morphology was also observed from SEM and TEM. Furthermore, we have plotted the Guinier plot,  $\ln(I)$  vs.  $q^2$  over a broad range which indicates the presence of monodispersed pore size. The Guinier approximation,  $\ln I = \ln I_0 - q^2 R_g^2/3$ , was used to estimate the particle radius of gyration ( $R_g$ ), where  $I$  is the scattering intensity and  $I_0$  is the extrapolated scattering intensity. The  $R_g$  was calculated from the slope of the lower part Guinier regime and found to be 2, 2.16, and 2.39 nm for TFG-EDA, TFG-DETA, and TFG-TETA, respectively. It was also observed that the gyration of micro voids increases with increased diamine length, which is in good agreement with theoretical approximation.<sup>59</sup> The Guinier curve of TFG-EDA, TFG-DETA, and TFG-TETA has a large linear region indicating the presence of monodispersed porous morphology. To characterize the porous structure of synthesized COFs, the scattering curve was further analyzed by plotting the Porod plot with point-collimation [ $\ln\{q^4 I(q)\} = \ln K_p + \alpha^2 q^2$ ], by plotting between  $q^2$  vs.  $\ln q^4 I$  (shown in Fig. 3I). For all COFs,  $\sigma$  was observed to be  $\sim 0.4$  to  $0.7$ , suggesting the smoother pore surface with almost no deviation, further assuring the presence of a sharp pore boundary without any fractal surface.<sup>60,61</sup> Overall, the SAXS

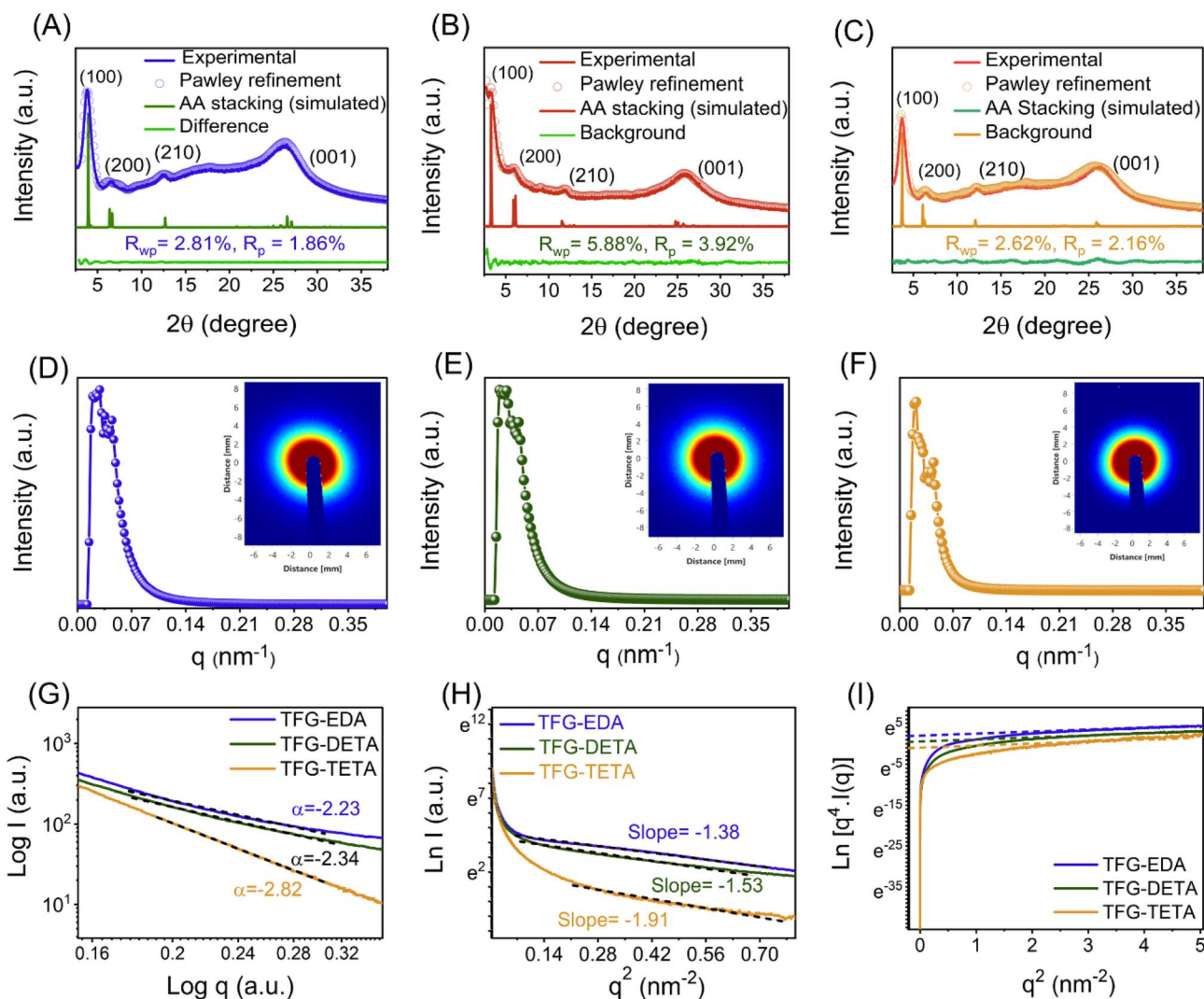


Fig. 3 Characterization of TFG-EDA, TFG-DETA, and TFG-TETA thin films. (A–C) the PXRD pattern with experimental PXRD pattern (circles), Pawley refinement plot (line), and difference between experimental and simulated profiles. (D–F) SAXS scattering data of TFG-EDA, TFG-DETA, and TFG-TETA, respectively. The inset figures in (A–C) show the 2D scattering image of corresponding COFs. (G) Corresponding log–log plot of SAXS profile, (H) Guinier plot. (I) Porod plot with point-collimation, which shows a linear plateau without any deviation.

analysis suggests the higher crystallinity, uniform, and stable porous architecture of synthesized COFs, which could be beneficial for molecular separation applications.

### 2.3 Surface charge and mechanical properties of COF nanofilm membranes

Zeta potential and water contact angle measurements were performed to evaluate the surface charge and water wettability properties of COF membranes. Surface charge is a crucial factor affecting the molecular separation and fouling properties of membranes. The streaming potential of COF membranes was studied using an electrokinetic analyzer over a pH range of 2–9. As shown in Fig. 4A, the isoelectric point (IEP) of TFG-EDA, TFG-DETA and TFG-TETA membranes were found to be at pH 3.4, 4.5, and 4.9, respectively. A positive zeta potential value at lower pH can be attributed to the protonation of the imine and –NH– groups of the COF frameworks, while a negative zeta potential at

higher pH can be explained by deprotonation and the availability of negative charges on the >C=O groups of the COF skeleton. Additionally, a slight increment in the IEP value and positive streaming potential was observed, which could be explained by the presence of more –NH groups in the order of EDA > DETA > TETA. In conclusion, all COF membrane exhibit positive charges at pH ~4 to 4.5 and negative charges when the pH is above ~4.6, as evident from the zeta potential analysis. The water contact angle was used to assess the surface wettability of COF membranes, and the results indicate that all COF membranes possess a hydrophilic surface. As shown in Fig. 4B, the contact angle of TFG-EDA, TFG-DETA, and TFG-TETA was found to be 56, 49, and 43°, respectively. The lower contact angle for TFG-TETA can be attributed to the presence of more polar groups and –NH moieties on its framework, which enhances the water affinity *via* hydrogen bonding.<sup>62</sup>



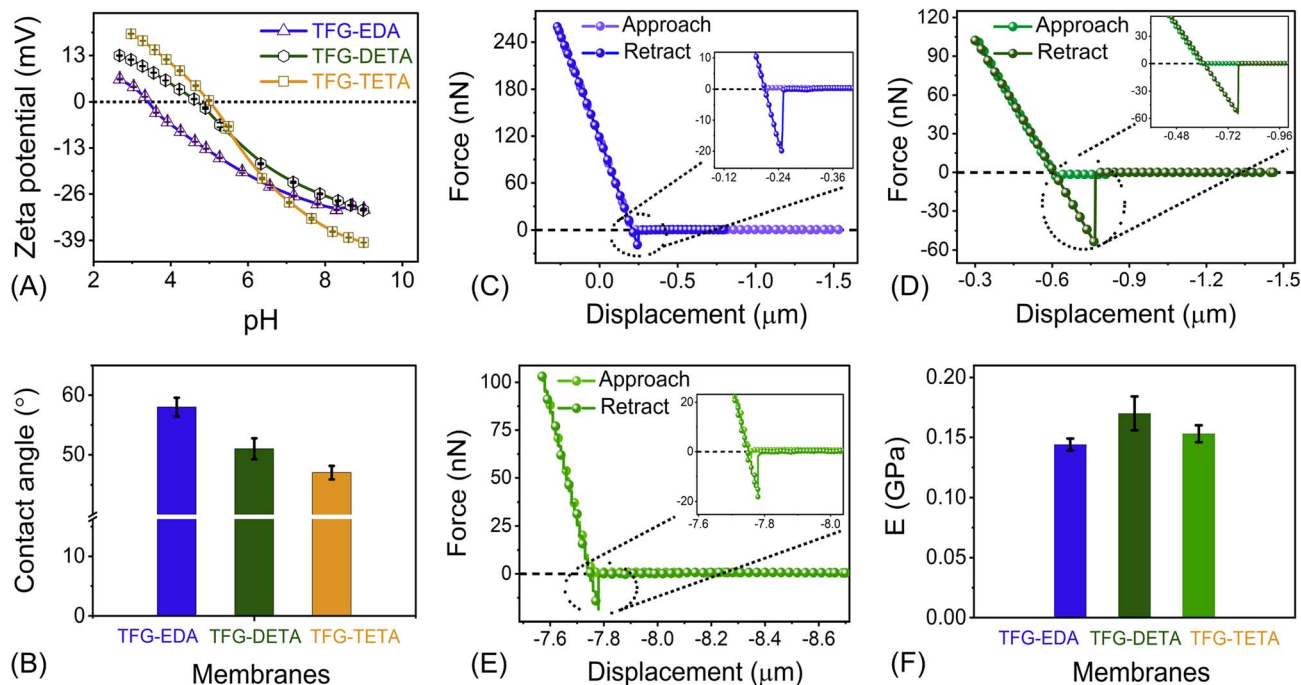


Fig. 4 Surface and mechanical properties of COF membranes. (A) Zeta potential of COF membrane as a function of pH, (B) water contact angle. Force-displacement curves obtained from the AFM based nanoindentation experiments (C) TFG-EDA, (D) TFG-DETA, (E) TFG-TETA, and (F) modulus of COF membranes.

Furthermore, stacking of a higher number of COF nanosheets endows the COF membranes with higher hydrophilicity.

To evaluate the fouling resistance of the COF membranes, a protein adsorption study was conducted using BSA, and the results are presented in Fig. S14A (ESI<sup>†</sup>). The amount of BSA adsorbed on TFG-EDA, TFG-DETA, and TFG-TETA membranes was found to be 24.83, 23.17, and 20.67  $\mu\text{g cm}^{-2}$ , respectively. To visualize the adsorbed BSA protein, fluorescein isothiocyanate conjugate-BSA was allowed to adhere to the membrane surface for a specified period, and the resulting fluorescence images are shown in Fig. S14C–E (ESI<sup>†</sup>). The images indicated minimal protein adsorption, resulting in lower fluorescence intensity. This suggests that COF membranes possess strong resistance against the BSA foulant, which could be due to the increased hydrophilicity, negative zeta potential, and the presence of abundant secondary amine (–NH) groups, resulting in a buffered hydrated layer on the COF surface that resists protein adsorption.<sup>63</sup>

To ensure applicability in industrial and real-field settings, the mechanical properties of thin film COF membranes are crucial. AFM-based nanoindentation experiments have been successfully used to assess the nanomechanical properties of various materials, including graphene, 2D boron nitride, molybdenum sulfide, *etc.*<sup>64,65</sup> We performed similar experiments to investigate the nanomechanical properties of interfacially crystallized COF thin films of  $\sim 105$  nm thickness on a cleaned Si wafer. The resulting force–displacement curves are shown in Fig. 4C–E. A schematic representation of a thin films behavior during the nanoindentation experiment is provided in Fig. S15 (ESI<sup>†</sup>). Quantitatively, the elastic modulus of COF thin

film was estimated by fitting the low deflection portion of the retract curve of the force–displacement curve ( $F$ – $S$  curve) using the JKR model. The resulting modulus values for TFG-EDA, TFG-DETA, and TFG-TETA films were  $0.144 \pm 0.005$ ,  $0.17 \pm 0.014$  and  $0.153 \pm 0.007$  GPa, respectively. Slight variations in the elastic modulus for different COF films can be attributed to their distinct molecular architecture/composition, with a higher elastic modulus resulting from a covalently bonded framework, presence of crystalline domains, and higher crystallinity that requires more load to destroy the internal architecture and tip penetration. These observations confirmed that the fabricated COF films showed good mechanical stability, making them suitable for various nanofiltration applications.

## 2.4 Permeation and separation performance analysis

**2.4.1 Molecular weight cut-off (MWCO) analysis.** To estimate the pore size of COF membranes before using them for permeation and filtration applications, we employed the neutral-solute (PEG) transport method. Different molecular weight PEG solutions were passed through the COF membrane, and based on the rejection analysis, we calculated the pore size and distribution of the COF membrane. The results are presented in Fig. S16 (ESI<sup>†</sup>). The MWCO of TFG-EDA, TFG-DETA and TFG-TETA membranes were found to be 0.38, 0.57 and 0.71 kDa, respectively. The pore size was determined based on the Stoke diameter of PEG solutes, and the sizes were found to be 0.91, 1.14 and 1.29 nm for TFG-EDA, TFG-DETA, and TFG-TETA, respectively. The PEG exclusion data were fitted to a sigmoidal curve model, and the MWCO probability

distributions indicated that the COF membranes exhibited a narrow pore size distribution. The presence of sub-2 nm pores with narrow distribution and enhanced hydrophilicity in the COF membranes improves the permeability and facilitates the rejection of various small molecules.

**2.4.2 Organic solvent nanofiltration.** The developed COF membranes were extensively characterized and found to have uniform, nanosized porous morphology, narrow pore size distribution, and  $\pi$ - $\pi$  stacking arrangement, making them suitable for separation applications. Before conducting the OSN experiments, the stability of COF membranes was assessed by immersing a piece of COF membrane in DMF and hexane for 48 h. As anticipated, the crystallinity and morphology of the COFs remained intact, indicating the robustness and stability of COF membranes in organic mediums (Section 12.1, Fig. S17, ESI†). To achieve a balance between solvent permeation and molecular rejection, the thickness of the selective layer plays a crucial role. Therefore, we evaluated the water permeance and dye rejection with COF membranes of different thickness. As shown in Fig. S18 (ESI†), the thinner TFG-EDA (~20 nm) membrane exhibited a higher water permeance (~680 L m<sup>-2</sup> h<sup>-1</sup> bar<sup>-1</sup>) but lower congo red (CR) rejection (~40%). As the layer thickness increased, the water permeance decreased while the CR rejection sharply increased. This is because a thicker membrane provides greater resistance to molecule transport and increased pore tortuosity.<sup>66</sup> Among all tested membranes, those with ~120 nm layer thickness demonstrated the most promising trade-off between water permeance and CR rejection. Hence, COFs membrane with ~120 nm thickness was selected for further OSN studies. To assess the pressure-dependent

filtration properties and the compression resistance of the COF layers, we performed the solvent permanence experiment by varying the pressure range from 1 to 7 bar. The results shown in Fig. S19 (ESI†), revealed no significant decrease in water flux was observed, and the water flux increased linearly with applied pressure. These findings indicate that the porosity within the COF layer remained unchanged even with increased compression. The COF membrane exhibited excellent mechanical properties and could withstand high filtration pressures, as evidenced by nanoindentation experiments. No surface cracks or pinholes were observed, and the surface remained flexible and uniform after the filtration with 7 bar applied pressure, demonstrating the robustness of the COF layer (Fig. S20A–C, ESI†). Furthermore, XRD analysis confirmed that the COF membrane retained its crystallinity after the pressure-dependent filtration test, highlighting its unique structural and mechanical stability (Fig. S20D–F, ESI†). The OSN experiment with COF membranes was conducted under different pressure at ambient temperature and the results are shown in Fig. 5. The water filtration studies revealed a linear increment of pure water flux with applied pressure, indicating that the porosity and structural integrity of COF membranes remained intact with increasing compression. The water flux of TFG-EDA, TFG-DETA, and TFG-TETA was 531, 658, and 720 L m<sup>-2</sup> h<sup>-1</sup> (at 3 bar), respectively. The higher flux for TFG-TETA than TFG-EDA and TFG-DETA can be attributed to its increased pore diameter and enhanced hydrophilicity, providing less flow resistance. The obtained water flux is comparatively higher than previously reported NF membranes, and the reason can be explained by its higher surface hydrophilicity and ordered porous morphology,

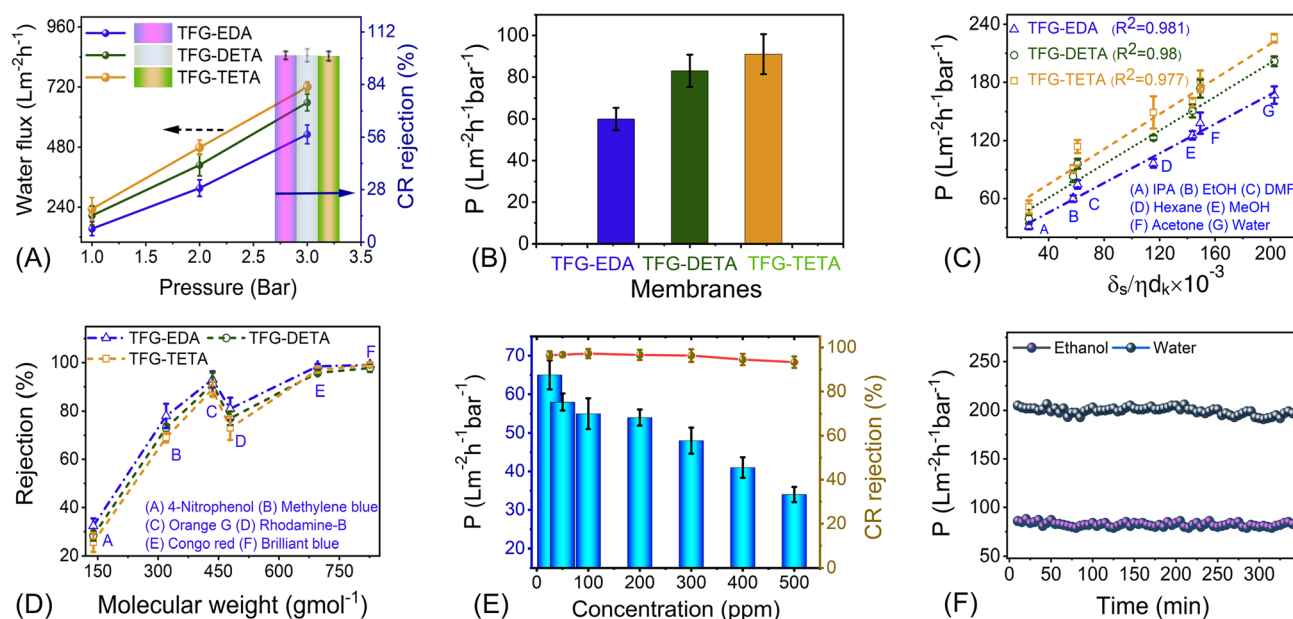


Fig. 5 OSN performance of COF membranes. (A) Pure water flux at different pressures and congo red rejection (50 ppm) at 3 bar of applied pressure. (B) Pure ethanol permeance. (C) A phenomenological model for pure solvent permeance and is related to solubility parameters, viscosity, and molar diameter of solvents. (D) Molecular rejection performance of different size/charge solutes in ethanol with 50 ppm concentration. (E) Effect of concentration of CR on permeance and rejection. (F) Long-term solvent permanence test of ethanol and water using TFG-DETA membrane.



which facilitates the solvent molecules diffusion process through the COF membrane. Compared with aromatic linkers, these COF frameworks possess aliphatic diamines that enhance structural flexibility and could provide a loose nanofiltration channel with a less tortuous path for permeation.<sup>67</sup> In addition, all the COF membranes exhibit more than 98% congo red (CR) rejection at 3 bar.

To further showcase the potential of COF membranes, we conducted OSN experiments using various polar and nonpolar solvents. Before the test, the membranes were soaked in the respective solvents, and filtration data were collected after achieving stable permeance. Initially, we tested the pure ethanol permeance through the membrane, which was found to be 60, 83, and 91 L m<sup>-2</sup> h<sup>-1</sup> bar<sup>-1</sup> for TFG-EDA, TFG-DETA, and TFG-TETA membranes, respectively. Like water flux, the ethanol flux also exhibited a linear increment with applied pressure for the TFG-DETA membrane, demonstrating the robustness of the COF layer on the porous support (Fig. S21, ESI†). Compared to traditional NF membranes, such as polyamide, polyacrylonitrile, metal-organic framework, and graphene, our designed COF membranes exhibited higher ethanol permeance. This can be attributed to the COF's flexible molecular architecture, unique surface functionality, structural persistence, and abundant narrowed micropores. Moreover, it should be noted that the kinetic diameter of the ethanol molecule is around ~0.4 nm, which is lower than the membrane pore diameter.<sup>68</sup>

We also conducted permeance tests for various solvents, such as methanol (MeOH), ethanol (EtOH), isopropanol (IPA), hexane, acetone, dimethylformamide (DMF), and water, and the results are depicted in Fig. 5C. Highest and lowest permeance values were observed for water and isopropanol, respectively. Interestingly, acetone exhibited lower permeance despite having a much lower viscosity than water. Thus, we assume that viscosity is not the only factor affecting the flow parameter. Standard continuum models for solvent transport in NF membranes generally assume that viscosity is the sole liquid parameter that affects permeance. However, for NF membranes, especially for OSN, permeance can be influenced by many factors, in addition to viscosity. Buekenhoudt *et al.* developed a phenomenological model relating the diameter of the solvent molecule, dynamic viscosity, and solubility parameters for the permeance of various solvents in NF membranes.<sup>68</sup> Livingston and co-workers successfully adopted this model for thin polyamide NF membranes.<sup>68,69</sup> This model particularly focuses on exploring the correlation of three parameters: the interaction between solvent and membrane, the effect of excluded volume on the transportation of species, and the momentum diffusion of solvents through the membrane. A comparison among different models was obtained (Fig. S22, ESI†), suggesting that the solvent flux is attributed to the combined effects of the total Hansen solubility parameter, kinetic diameter, and viscosity of solvents. This phenomenological model utilizes various parameters, including solubility parameter, viscosity, and kinetic diameter, where the permeance scales linearly with the solvent parameters  $k\delta_s/\eta d_k$ . The proposed equation is given below:

$$p = \frac{k\delta_s}{\eta d_k} \quad (1)$$

where  $k$  is the proportionality constant that describes the solute transport parameter,  $\delta_s$  is the Hansen solubility parameter,  $\eta$  is the solvent viscosity, and  $d_k$  is the kinetic diameter of solvents. Our solvent permeance results are well fitted with the above model ( $R^2 \sim 0.98$ ), suggesting that the transport phenomenon of solvent molecules through the COFs membrane is influenced by both COF-solvent interactions and its kinetic diameter and viscosity.

**2.4.3 Molecular separation performance.** We evaluated the rejection performance of COF membranes using different-sized and charged solutes (Table S4, ESI†) with a concentration of 50 ppm in ethanol at 3 bar of applied pressure. The permeance was collected after reaching a stable flux, and the percentage of rejection was calculated using a UV-vis spectrophotometer. A slight decrement in rejection percentage for TFG-TETA compared to TFG-EDA, implying a strong dependency between the porosity of COF membranes and rejection performance. The COF membrane exhibited remarkable permeance with high dye separation efficiency. The rejection of dyes by the COF membrane can be attributed to three main mechanisms: (a) adsorption of dyes on COF substrate, (b) size sieving effect from the nanochannels of COF membranes, and (c) Donnan exclusion, which describes the electrostatic interaction between charged dye molecules and negatively charged surface observed from zeta potential. The presence of aromatic rings and polar groups on COFs could facilitate the dye adsorption, which in turn can lead to loss in rejection performance and long-term applicability. Moreover, it is important to mention that under pressurized conditions, a smaller portion of solutes is adsorbed on the membrane surface, and it can be easily removed using a simple washing step. Also, in the case of stronger adsorption, the dye concentration in retentate remains unchanged with increasing permeation. Therefore, to determine the separation mechanism of the COF membrane, we conducted a control experiment using 50 ppm of Congo red, and the retentate was collected at different permeate volumes (5, 10, 20 mL). A significant increase in the retentate concentration was observed (Fig. S23, ESI†), indicating that the separation mechanism is not due to adsorption. From the MWCO analysis, we found that the pore size of TFG-EDA, TFG-DETA, and TFG-TETA membranes was 0.91, 1.14 and 1.29 nm, respectively. The hydrated diameter of dye molecules is much larger than the obtained pore size; thus, the rejection of dye molecules is dominated by the size-sieving effect. However, due to its negative zeta potential value, the electrostatic interaction of dye molecules with the membrane cannot be neglected. Therefore, we conducted dye rejection experiments using dyes of almost similar molecular size but with different charges (in this case, rhodamine B (RhB) is positively charged, and orange G is negatively charged). We observed lower rejection for RhB compared to orange G, even though orange G has a smaller size, confirming that the rejection performance can also be influenced by Donnan exclusion. Positively charged RhB is attracted by the negatively charged COF surface, resulting in higher

permeance with lower rejection (Fig. S24, ESI†). As a result, we conclude that the molecular size-sieving effect and Donnan effect are jointly associated with the rejection of dye molecules, while ethanol, having a diameter of  $\sim 0.4$  nm, can easily pass through the COF membranes.

Congo red rejection was performed by varying the concentration from 50 ppm to 500 ppm, using TFG-DETA as the model membrane to further demonstrate the advantage of the designed COF membranes. TFG-DETA membrane showed superior performance with more than 90% rejection up to 500 ppm without compromising permeation properties. The lower permeance with dye solution compared to pure ethanol can be attributed to the concentration polarization.<sup>70</sup> This leads to the deposition of dye molecules on the membrane surface and reduces the permeation. However, the ethanol permeance from the dye solution was comparable or better than previously reported literature, indicating superior performance. Furthermore, the OSN performance of TFG-EDA, TFG-DETA, and TFG-TETA membranes was compared with previously reported state-of-the-art NF membranes (shown in Fig. 6A, Table S5, ESI†). Our COF membranes exhibited simultaneously higher ethanol permeance and superior molecular rejection, exceeding the upper bound of previously reported NF membranes.

**2.4.4 Long-term filtration and antifouling efficacy.** In addition to permeance and rejection performance, the long-

term operational stability of COF membranes with different solvents is a crucial parameter for OSN performance. To demonstrate this, we performed a long-term solvent permeance test using ethanol and water as solvents. After reaching a steady flux, we collected filtration data and found that the TFG-DETA membrane showed superior operational stability for several hours of filtration. There was no significant decline or abrupt increment in permeance value, indicating the stability and absence of surface cracks or pinholes on the membrane surface. To ensure the stability of the COF layer, we performed a sequential stability test (Fig. 6B), which showed that the pure water permeance and CR rejections value did not decrease significantly over a 24 h operational cycle. The structural and morphological stability of TFG-DETA membrane was assessed after 24 h of sequential OSN performance test. The results shown in Fig. 6C and D, indicate no surface defects or structural changes after OSN operation, signifying the stability of the COF membrane towards long-term OSN filtration test. Additionally, we collected the retentate after the long-term filtration cycle and lyophilized it but did not observe any trace of solid COFs product, further assuring the stability of the COF layer on the PET membrane support. The long-term stability of the COF membrane was evaluated by conducting multiple cycles of dye rejection tests. Fig. S26 (ESI†) shows that the COF membranes consistently maintained dye rejection with flux recovery

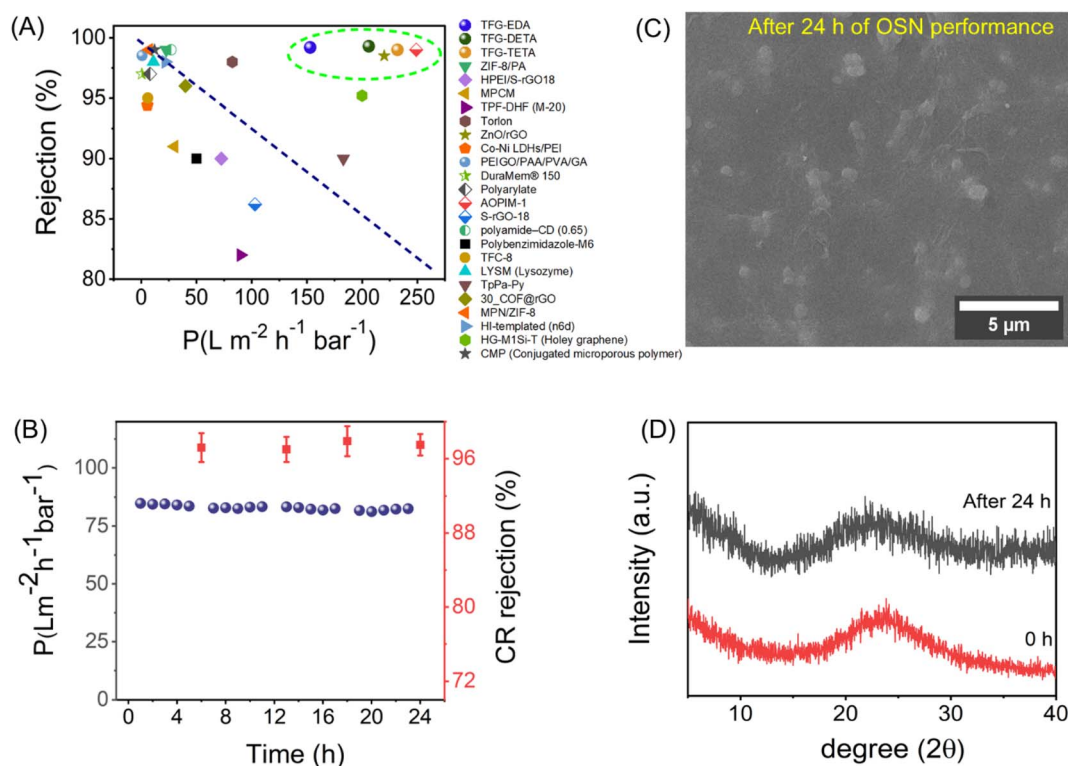


**Fig. 6** COFs membrane performance comparison and rejection and long-term stability analysis. (A) Filtration performance comparison of COF membranes with the state-of-the-art NF membranes for water purification. (B) stability test of the membrane using long-term OSN experiment in a sequential manner (after each 4 hours of ethanol permeance a rejection test with congo red was performed). The ethanol permeance-congo red rejection cycle was repeated for four cycles on the same TFG-DETA membrane. (C) FESEM and (D) PXRD characterization of TFG-DETA membrane post 24 h sequential permeation-rejection tests.

throughout ten consecutive cycles. This indicates that the membranes retained their selective separation properties. Furthermore, the long-term dye rejection performance was assessed over an extended period of 14 hours, and the results demonstrate no significant change in the rejection performance (Fig. S27, ESI†). This stable permeance with long-term rejection illustrates the COF membrane's unique stable morphology, mechanical stability, microporosity, and chemical stability towards enhanced long-term stability in filtration performance.

Apart from structural and morphological stability, fouling on the membrane surface is another common and undesirable phenomenon in the case of NF membranes. Foulants can spontaneously adhere to the membrane surface, resulting in a deterioration of membrane performance. To verify the fouling resistance of COF membranes, a dynamic BSA filtration test was conducted using 50 mg L<sup>-1</sup> solution and the results are shown in Fig. S28A (ESI†). As expected, all COF membranes exhibited almost complete BSA rejection (>98%) due to the larger hydrodynamic size of BSA molecules compared to the COF pores. A higher flux recovery ratio was observed for all COF membranes, indicating their superior fouling resistance. After the cleaning cycle, COF membranes could recover ~92% of their initial flux. The major causes of total fouling are adsorption, deposition, and pore-clogging with BSA molecules on the membrane surface. To further examine the antifouling mechanism, we have calculated different fouling resistance parameters such as total fouling ( $R_t$ ), reversible fouling ( $R_r$ , removable), and irreversible fouling ( $R_{ir}$ , irremovable).<sup>71</sup> As shown in Fig. S28B (ESI†), the COF membrane displays higher reversible fouling, signifying a weak interaction of BSA molecules with the COF surface. In summary, the designed COF membranes exhibit superior OSN, rejection, long-term solvent filtration, and anti-fouling performance, which is beneficial for industrial applications.

### 3. Conclusions

In summary, we synthesized and fabricated COF membranes for OSN applications. The COF membranes were synthesized through liquid-liquid interfacial polymerization, using different aliphatic diamines bridged covalently to modify their pore size and chemistry. We found that the use of aliphatic linear diamines resulted in flexible COFs with comparable mechanical properties to those synthesized with conventional aromatic diamines. By varying the diamine chain length, we were able to tune the pore size and, therefore, the solute and solvent transport phenomenon. The growth process of COF nanofilms was controlled by varying polymerization time and analyzed using various techniques to confirm the formation of  $\beta$ -Ketoenamine bonds and the complete reaction of both monomers at the interface. The fabricated COF membrane showed superior solvent permeance, precise molecular separation, and substantial fouling resistance in both static and dynamic conditions. Additionally, the COF membranes exhibited good operational stability for 24 hours of continuous solvent permeance and multicycle filtration without any surface defects or disruption in permeance activity. Overall, this study

demonstrates the potential of linear diamine-based COF membranes for various membrane filtration applications, particularly in water purification and organic solvent nano-filtration. The findings of this work may contribute to the development of envisioned COF-based NF membranes for various separation applications.

### Data availability

All data are available in the main text or ESI.†

### Author contributions

B. Mishra: methodology, validation, formal analysis, investigation, data curation, writing – original draft. B. P. Tripathi: conceptualization, resources, writing – review & editing, supervision, funding acquisition.

### Conflicts of interest

The authors declare no conflict of interest.

### Acknowledgements

BPT sincerely acknowledges funding support from the Department of Science and Technology, Gov. of India (DST/TMD/EWO/WTI/2K19/EWFH/2019/73). BM is grateful to the Ministry of Education, India for the Senior Research Fellowship. Authors acknowledge the High-performance computing (HPC) facility, Central Research facility and Nano Research facility at IIT Delhi for Materials studio, AFM, SEM, XPS, TEM, and other characterizations.

### References

- 1 D. S. Sholl and R. P. Lively, *Nature*, 2016, **532**, 435–437.
- 2 R. P. Lively and D. S. Sholl, *Nat. Mater.*, 2017, **16**, 276–279.
- 3 S. Jhulki, A. M. Evans, X.-L. Hao, M. W. Cooper, C. H. Feriante, J. Leisen, H. Li, D. Lam, M. C. Hersam, S. Barlow, J.-L. Brédas, W. R. Dichtel and S. R. Marder, *J. Am. Chem. Soc.*, 2020, **142**, 783–791.
- 4 P. Marchetti, M. F. Jimenez Solomon, G. Szekely and A. G. Livingston, *Chem. Rev.*, 2014, **114**, 10735–10806.
- 5 M. A. Shannon, P. W. Bohn, M. Elimelech, J. G. Georgiadis, B. J. Mariñas and A. M. Mayes, *Nature*, 2008, **452**, 301–310.
- 6 L. Huang, J. Chen, T. Gao, M. Zhang, Y. Li, L. Dai, L. Qu and G. Shi, *Adv. Mater.*, 2016, **28**, 8669–8674.
- 7 T. Hoare, J. Santamaria, G. F. Goya, S. Irusta, D. Lin, S. Lau, R. Padera, R. Langer and D. S. Kohane, *Nano Lett.*, 2009, **9**, 3651–3657.
- 8 W. Xie, T. Li, A. Tiraferri, E. Drioli, A. Figoli, J. C. Crittenden and B. Liu, *ACS Sustainable Chem. Eng.*, 2021, **9**, 50–75.
- 9 L. Gui, J. Dong, W. Fang, S. Zhang, K. Zhou, Y. Zhu, Y. Zhang and J. Jin, *Nano Lett.*, 2020, **20**, 5821–5829.
- 10 G. Han, T.-S. Chung, M. Weber and C. Maletzko, *Environ. Sci. Technol.*, 2018, **52**, 3676–3684.



- 11 W. Zhang, H. Xu, F. Xie, X. Ma, B. Niu, M. Chen, H. Zhang, Y. Zhang and D. Long, *Nat. Commun.*, 2022, **13**, 471.
- 12 M. Elimelech and W. A. Phillip, *Science*, 2011, **333**, 712–717.
- 13 P. Vandezande, L. E. M. Gevers and I. F. J. Vankelecom, *Chem. Soc. Rev.*, 2008, **37**, 365–405.
- 14 J. C.-T. Lin and A. G. Livingston, *Chem. Eng. Sci.*, 2007, **62**, 2728–2736.
- 15 M.-B. Wu, F. Yang, J. Yang, Q. Zhong, V. Körstgen, P. Yang, P. Müller-Buschbaum and Z.-K. Xu, *Nano Lett.*, 2020, **20**, 8760–8767.
- 16 Q. Yang, Y. Su, C. Chi, C. T. Cherian, K. Huang, V. G. Kravets, F. C. Wang, J. C. Zhang, A. Pratt, A. N. Grigorenko, F. Guinea, A. K. Geim and R. R. Nair, *Nat. Mater.*, 2017, **16**, 1198–1202.
- 17 T. Gao, H. Wu, L. Tao, L. Qu and C. Li, *J. Mater. Chem. A*, 2018, **6**, 19563–19569.
- 18 J. R. McCutcheon and M. Elimelech, *J. Membr. Sci.*, 2006, **284**, 237–247.
- 19 S. Gao, Y. Zhu, Y. Gong, Z. Wang, W. Fang and J. Jin, *ACS Nano*, 2019, **13**, 5278–5290.
- 20 A. P. Côté, A. I. Benin, N. W. Ockwig, M. O’Keeffe, A. J. Matzger and O. M. Yaghi, *Science*, 2005, **310**, 1166–1170.
- 21 H. S. Sasmal, A. Kumar Mahato, P. Majumder and R. Banerjee, *J. Am. Chem. Soc.*, 2022, **144**, 11482–11498.
- 22 Y. Shi, J. Yang, F. Gao and Q. Zhang, *ACS Nano*, 2023, **17**, 1879–1905.
- 23 P. She, Y. Qin, X. Wang and Q. Zhang, *Adv. Mater.*, 2022, **34**, 2101175.
- 24 X. Liu, G. J. H. Lim, Y. Wang, L. Zhang, D. Mullangi, Y. Wu, D. Zhao, J. Ding, A. K. Cheetham and J. Wang, *Chem. Eng. J.*, 2021, **403**, 126333.
- 25 Z. Li, X. Feng, Y. Zou, Y. Zhang, H. Xia, X. Liu and Y. Mu, *Chem. Commun.*, 2014, **50**, 13825–13828.
- 26 F. Yu, W. Liu, S.-W. Ke, M. Kurmoo, J.-L. Zuo and Q. Zhang, *Nat. Commun.*, 2020, **11**, 5534.
- 27 J. Sun, Y. Xu, Y. Lv, Q. Zhang and X. Zhou, *CCS Chem.*, 2023, **5**, 1259–1276.
- 28 S. Kandambeth, K. Dey and R. Banerjee, *J. Am. Chem. Soc.*, 2019, **141**, 1807–1822.
- 29 D. B. Shinde, G. Sheng, X. Li, M. Ostwal, A.-H. Emwas, K.-W. Huang and Z. Lai, *J. Am. Chem. Soc.*, 2018, **140**, 14342–14349.
- 30 D. B. Shinde, L. Cao, A. D. D. Wonanke, X. Li, S. Kumar, X. Liu, M. N. Hedhili, A.-H. Emwas, M. Addicoat, K.-W. Huang and Z. Lai, *Chem. Sci.*, 2020, **11**, 5434–5440.
- 31 T. Yang, H. Lin, X. Zheng, K. P. Loh and B. Jia, *J. Mater. Chem. A*, 2017, **5**, 16537–16558.
- 32 Z. Li, T. He, Y. Gong and D. Jiang, *Acc. Chem. Res.*, 2020, **53**, 1672–1685.
- 33 S. Bi, C. Yang, W. Zhang, J. Xu, L. Liu, D. Wu, X. Wang, Y. Han, Q. Liang and F. Zhang, *Nat. Commun.*, 2019, **10**, 2467.
- 34 J. Liu, G. Han, D. Zhao, K. Lu, J. Gao and T.-S. Chung, *Sci. Adv.*, 2020, **6**, eabb1110.
- 35 J. Liu, D. Hua, Y. Zhang, S. Japip and T.-S. Chung, *Adv. Mater.*, 2018, **30**, 1705933.
- 36 M. Matsumoto, R. R. Dasari, W. Ji, C. H. Feriante, T. C. Parker, S. R. Marder and W. R. Dichtel, *J. Am. Chem. Soc.*, 2017, **139**, 4999–5002.
- 37 L.-Y. Chen, Y.-N. Gai, X.-T. Gai, J. Qin, Z.-G. Wang, L.-S. Cui, H. Guo, M.-Y. Jiang, Q. Zou, T. Zhou and J.-G. Gai, *Chem. Eng. J.*, 2022, **430**, 133024.
- 38 J.-Y. Yue, X.-H. Liu, B. Sun and D. Wang, *Chem. Commun.*, 2015, **51**, 14318–14321.
- 39 M. Matsumoto, L. Valentino, G. M. Stiehl, H. B. Balch, A. R. Corcos, F. Wang, D. C. Ralph, B. J. Mariñas and W. R. Dichtel, *Chem*, 2018, **4**, 308–317.
- 40 M. F. Pantano, E. Missale, L. Gazzato, R. Pilot, F. Sedona, G. Speranza and M. Frascioni, *Mater. Today Chem.*, 2022, **26**, 101007.
- 41 A. López-Magano, A. E. Platero-Prats, S. Cabrera, R. Mas-Ballesté and J. Alemán, *Appl. Catal., B*, 2020, **272**, 119027.
- 42 C. R. DeBlase, K. E. Silberstein, T.-T. Truong, H. D. Abruña and W. R. Dichtel, *J. Am. Chem. Soc.*, 2013, **135**, 16821–16824.
- 43 Q. Li, X. Lan, G. An, L. Ricardez-Sandoval, Z. Wang and G. Bai, *ACS Catal.*, 2020, **10**, 6664–6675.
- 44 Z. Lei, Q. Yang, Y. Xu, S. Guo, W. Sun, H. Liu, L.-P. Lv, Y. Zhang and Y. Wang, *Nat. Commun.*, 2018, **9**, 576.
- 45 A. R. Abdellah, H. N. Abdelhamid, A.-B. A. A. M. El-Adasy, A. A. Atalla and K. I. Aly, *J. Environ. Chem. Eng.*, 2020, **8**, 104054.
- 46 Y. Zhi, P. Shao, X. Feng, H. Xia, Y. Zhang, Z. Shi, Y. Mu and X. Liu, *J. Mater. Chem. A*, 2018, **6**, 374–382.
- 47 L. Valentino, M. Matsumoto, W. R. Dichtel and B. J. Mariñas, *Environ. Sci. Technol.*, 2017, **51**, 14352–14359.
- 48 N. A. Khan, R. Zhang, X. Wang, L. Cao, C. S. Azad, C. Fan, J. Yuan, M. Long, H. Wu, M. A. Olson and Z. Jiang, *Nat. Commun.*, 2022, **13**, 3169.
- 49 K. Dey, M. Pal, K. C. Rout, S. Kunjattu H, A. Das, R. Mukherjee, U. K. Kharul and R. Banerjee, *J. Am. Chem. Soc.*, 2017, **139**, 13083–13091.
- 50 S. Chandra, S. Kandambeth, B. P. Biswal, B. Lukose, S. M. Kunjir, M. Chaudhary, R. Babarao, T. Heine and R. Banerjee, *J. Am. Chem. Soc.*, 2013, **135**, 17853–17861.
- 51 L. Wang, B. Dong, R. Ge, F. Jiang and J. Xu, *ACS Appl. Mater. Interfaces*, 2017, **9**, 7108–7114.
- 52 S. Karak, S. Kandambeth, B. P. Biswal, H. S. Sasmal, S. Kumar, P. Pachfule and R. Banerjee, *J. Am. Chem. Soc.*, 2017, **139**, 1856–1862.
- 53 M. C. Daugherty, E. Vitaku, R. L. Li, A. M. Evans, A. D. Chavez and W. R. Dichtel, *Chem. Commun.*, 2019, **55**, 2680–2683.
- 54 L. Ascherl, E. W. Evans, M. Hennemann, D. Di Nuzzo, A. G. Hufnagel, M. Beetz, R. H. Friend, T. Clark, T. Bein and F. Auras, *Nat. Commun.*, 2018, **9**, 3802.
- 55 Z. Chen, J. Wang, M. Hao, Y. Xie, X. Liu, H. Yang, G. I. N. Waterhouse, X. Wang and S. Ma, *Nat. Commun.*, 2023, **14**, 1106.
- 56 R. L. Li, A. Yang, N. C. Flanders, M. T. Yeung, D. T. Sheppard and W. R. Dichtel, *J. Am. Chem. Soc.*, 2021, **143**, 7081–7087.
- 57 P. Schmidt, *J. Appl. Cryst.*, 1991, **24**, 414–435.
- 58 L. Feigin and D. I. Svergun, *Structure Analysis by Small-Angle X-Ray and Neutron Scattering*, Springer, 1987.

- 59 O. M. Londoño, P. Tancredi, P. Rivas, D. Muraca, L. M. Socolovsky and M. Knobel, in *Handbook of Materials Characterization*, ed. S. K. Sharma, Springer International Publishing, Cham, 2018.
- 60 G. Porod, *Kolloid-Z.*, 1951, **124**, 83–114.
- 61 J. T. Koberstein, B. Morra and R. S. Stein, *J. Appl. Cryst.*, 1980, **13**, 34–45.
- 62 H. Yang, H. Wu, Z. Yao, B. Shi, Z. Xu, X. Cheng, F. Pan, G. Liu, Z. Jiang and X. Cao, *J. Mater. Chem. A*, 2018, **6**, 583–591.
- 63 D. Xu, J. Zheng, X. Zhang, D. Lin, Q. Gao, X. Luo, X. Zhu, G. Li, H. Liang and B. Van der Bruggen, *Environ. Sci. Technol.*, 2022, **56**, 1927–1937.
- 64 R. Garcia, *Chem. Soc. Rev.*, 2020, **49**, 5850–5884.
- 65 O. M. McIntee, B. C. Welch, A. R. Greenberg, S. M. George and V. M. Bright, *Polymer*, 2022, **255**, 125167.
- 66 R. Shevate and D. L. Shaffer, *ACS Nano*, 2022, **16**, 2407–2418.
- 67 Y. Li, J. Zhu, S. Li, Z. Guo and B. Van der Bruggen, *ACS Appl. Mater. Interfaces*, 2020, **12**, 31962–31974.
- 68 A. Buekenhoudt, F. Bisignano, G. De Luca, P. Vandezande, M. Wouters and K. Verhulst, *J. Membr. Sci.*, 2013, **439**, 36–47.
- 69 S. Karan, Z. Jiang and A. G. Livingston, *Science*, 2015, **348**, 1347–1351.
- 70 M. Mulder and J. Mulder, *Basic Principles of Membrane Technology*, Springer science & business media, 1996.
- 71 B. Kwon, S. Lee, J. Cho, H. Ahn, D. Lee and H. S. Shin, *Environ. Sci. Technol.*, 2005, **39**, 732–739.